nature chemical biology

ARTICLES

https://doi.org/10.1038/s41589-018-0037-0

Dynamic coupling between conformations and nucleotide states in DNA gyrase

Aakash Basu[1,2,3], Matthew Hobson[3,4], Paul Lebel[1,2,8], Louis E. Fernandes[2,5,9], Elsa M. Tretter[6,10], James M. Berger[3,6] and Zev Bryant[2,7]*

Gyrase is an essential bacterial molecular motor that supercoils DNA using a conformational cycle in which chiral wrapping of >100 base pairs confers directionality on topoisomerization. To understand the mechanism of this nucleoprotein machine, global structural transitions must be mapped onto the nucleotide cycle of ATP binding, hydrolysis and product release. Here we investigate coupling mechanisms using single-molecule tracking of DNA rotation and contraction during *Escherichia coli* gyrase activity under varying nucleotide conditions. We find that ADP must be exchanged for ATP to drive the rate-limiting remodeling transition that generates the chiral wrap. ATP hydrolysis accelerates subsequent duplex strand passage and is required for resetting the enzyme and recapturing transiently released DNA. Our measurements suggest how gyrase coordinates DNA rearrangements with the dynamics of its ATP-driven protein gate, how the motor minimizes futile cycles of ATP hydrolysis and how gyrase may respond to changing cellular energy levels to link gene expression with metabolism.

Dynamic studies of diverse examples of molecular motors are needed to elucidate general principles of directed nanoscale motion and to uncover the specific physical mechanisms underlying cellular processes. DNA gyrase is a molecular motor belonging to the gyrase-Hsp90-MutL (GHL) family of ATPases[1], structurally and mechanistically distinct from P-loop motors[2] such as kinesin, myosin and F1 ATPase. Gyrase couples the hydrolysis of ATP with negative supercoiling of DNA[3,4] and affects diverse supercoiling-dependent genomic transactions[5] such as chromosome condensation, DNA replication and both global[6] and local[7] regulation of gene expression. The enzyme is essential for bacterial life and is an important target of antibiotic drugs[8].

For gyrase to function, separate chemical cycles of DNA cleavage and ATP hydrolysis must be coordinated with each other and with large conformational changes in the enzyme heterotetramer (Fig. 1) and the associated DNA. To provide a physical description of this process, we must define a cycle of global gyrase:DNA conformations and identify specific conformational transitions coupled to specific substeps in the ATP hydrolysis cycle. By characterizing the response of the motor to chemical and mechanical perturbations, we may rigorously probe models of energy transduction[9] and also establish how gyrase motor function can be regulated by changing cellular conditions[10,11].

A model based on sign inversion has been developed to explain the introduction of negative supercoils by DNA gyrase[3,12] (Fig. 1). The enzyme binds a segment of DNA known as the gate- or G-segment to its cleavage core and chirally wraps flanking DNA around the C-terminal domain (CTD) of the enzyme, leading to the capture of a second proximal segment of DNA, the transfer or T-segment, within the ATP-operated N-terminal entrance gate (N-gate) cavity. The trapped T-segment is then passed through a transient break in the G-segment, inverting the node between the two segments and introducing two negative supercoils. The passed T-segment is released by an opening in the exit gate. Decades of biochemical and structural investigations have established elements of this model for the gyrase mechanism, with detailed insights contributed by crystal structures of domains and subcomplexes[3] and by a recent low resolution cryo-EM view of the gyrase:DNA complex in a single trapped conformation[13]. However, dynamic measurements of active complexes are uniquely suited to defining the coordinated motions of the holoenzyme required for function.

Single-molecule measurements have identified conformational intermediates and ATP-dependent structural transitions in the enzymatic cycle of gyrase[4,14,15]. Three distinct nucleoprotein configurations—Ω, α and ν—were identified using rotor bead tracking (RBT), a method that measures real-time changes in the extension and rotation of a single stretched DNA molecule[15–17] (Fig. 1). In the Ω configuration, which dominates the kinetics of supercoiling, DNA appears to be bent around the CTDs without trapping a T-segment. Binding of two ATP molecules accelerates a global rearrangement of the nucleoprotein complex to form the α configuration, in which the DNA is chirally wrapped around the CTDs. Chiral wrapping, which prepares the enzyme for directional strand passage, is thus seen to be a multistep process modulated by ATP binding[16]. High-speed RBT further identified the ν configuration, a transient state in which sequestered DNA is apparently released from the CTDs of the complex after strand passage, before being recaptured to begin the next cycle[17].

Here we use RBT[16,18] and a new set of chemical and mechanical perturbations to dissect the complete mechanochemical cycle of DNA gyrase. ADP and the non-hydrolyzable analog adenylyl imidodiphosphate (AMPPNP) are used to probe the roles of nucleotide exchange and hydrolysis, and tension is used to stabilize the short-lived ν state, making it possible to study its geometry and ATP-coupled

[1]Department of Applied Physics, Stanford University, Stanford, CA, USA. [2]Department of Bioengineering, Stanford University, Stanford, CA, USA. [3]Department of Biophysics and Biophysical Chemistry, Johns Hopkins University School of Medicine, Baltimore, MD, USA. [4]Program in Molecular Biophysics, Johns Hopkins University, Baltimore, MD, USA. [5]Program in Biophysics, Stanford University, Stanford, CA, USA. [6]Department of Molecular and Cell Biology, University of California, Berkeley, Berkeley, CA, USA. [7]Department of Structural Biology, Stanford University Medical Center, Stanford, CA, USA. [8]Present address: Chan Zuckerberg Biohub, San Francisco, CA, USA. [9]Present address: Tempus, Inc., Chicago, IL, USA. [10]Present address: Nurix Inc., San Francisco, CA, USA. *e-mail: zevry@stanford.edu

dynamics. We find that ADP/ATP exchange specifically modulates the rate-limiting Ω-to-α transition, sensitizing the overall supercoiling rate to the [ADP]/[ATP] ratio. Preventing ATP hydrolysis specifically slows forward progress from the α state, mirroring effects on strand passage seen in yeast topoisomerase II (topo II)[19]. Finally, our characterization of the ν state leads to a model in which rapid conversion of ν to Ω serves to efficiently coordinate T-segment capture with closure of the entrance gate, helping to tightly link ATP consumption with supercoil introduction. Our results reveal that mechanochemical coupling, coordination and energy efficiency are achieved via a highly branched kinetic pathway, which may be representative of the GHL ATPase family to which gyrase belongs[20].

Results

The rotor bead tracking assay. We used RBT to examine structural dynamics in DNA gyrase (Fig. 1b). In this assay[15], a DNA molecule is stretched using a magnetic bead, and a polystyrene 'rotor' bead is attached to the side of the molecule. In the current implementation, the rotor is imaged from below using evanescent darkfield microscopy[17]. The angle of the rotor can be used to track changes in linking number as well as supercoils trapped by structural intermediates[16]. The height of the rotor above the surface can be measured simultaneously using evanescent nanometry[17], reporting on changes in DNA extension when DNA is bent or sequestered in the gyrase nucleoprotein complex[15,16].

The supercoiling reaction can be followed by recording the angle and the height (z) of the rotor as a function of time. In a typical example of a gyrase encounter with DNA under 0.8 pN tension in the presence of 1 mM ATP (Fig. 1c), z contracts as a result of the sequestration of DNA in the gyrase complex, while rotations accumulate as the enzyme processively introduces two negative supercoils per cycle. Under appropriate conditions, dwells in all previously observed conformations—ν, Ω and α—can be detected in the RBT assay used here. Ω can be identified as a dwell at ~0 rotations with extensive z contraction, while two variants of the α state, α_{1rot} and $\alpha_{1.7rot}$, can be identified as dwells at ~1 and ~1.7 rotations, respectively (Fig. 1d,e). Transient decreases in the amount of z contraction during angular dwells at ~0 rotations are also seen under some conditions and ascribed to dwells in the ν state (Fig. 1f) as discussed below.

Conformational isoforms trap different amounts of DNA. Before analyzing dynamics, we characterized the geometry and steady-state distributions of nucleoprotein conformations using an initial analysis that discards temporal information. As in earlier work[16], we have constructed two-dimensional histograms of paired (angle, z) values to visualize the structural properties and relative weights of

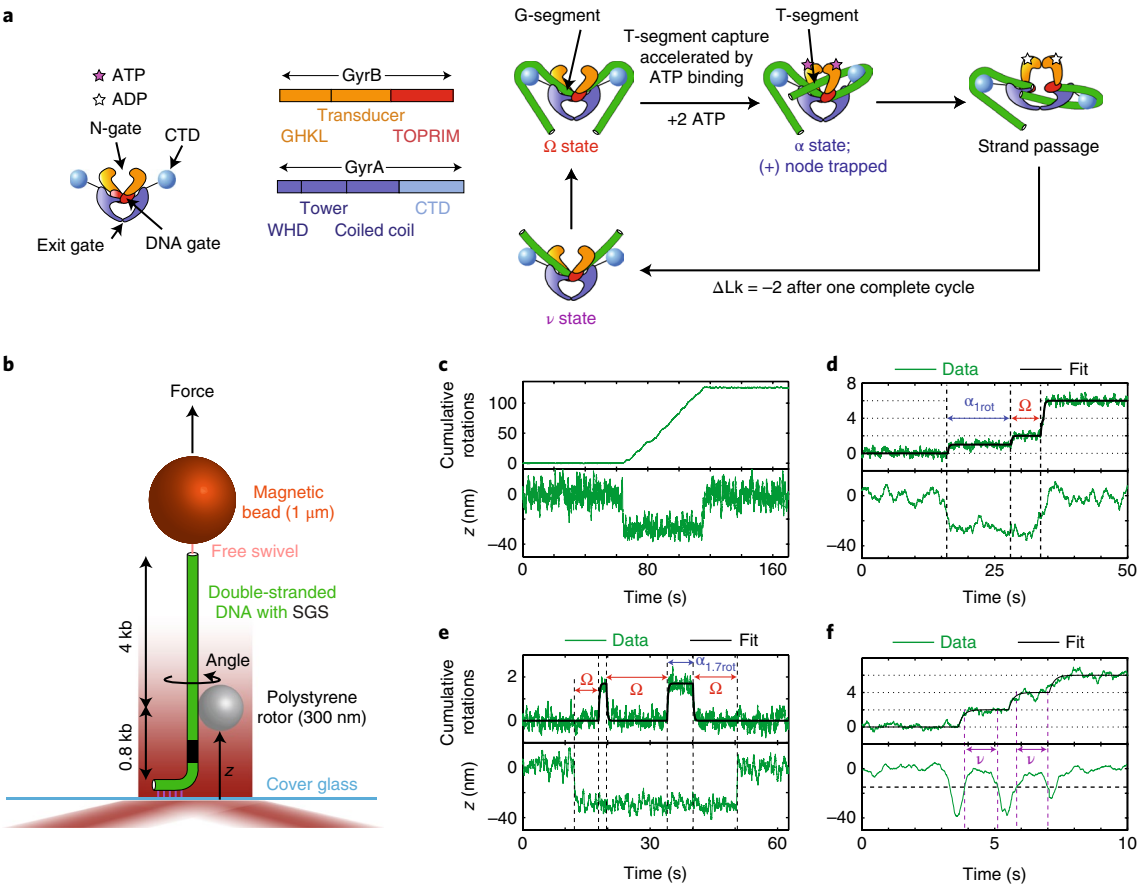

Fig. 1 | Gyrase mechanochemical cycle and single-molecule rotor bead tracking assay. a, Diagram of the gyrase tetramer showing approximate relationships between protein domains, block diagram of gyrase subunits, and schematic of the supercoiling reaction cycle. Labels indicate the GHKL (gyrase, Hsp90, histidine kinase, and MutL) ATPase domain, TOPRIM (topoisomerase-primase) domain, and WHD (winged-helix domain). ΔLk indicates change in linking number. **b**, Schematic of the RBT assay. A DNA template containing a strong gyrase site (SGS) is stretched using magnetic tweezers. Angle and z are measured by imaging the rotor from below using evanescent scattering[17]. **c**, Plot of cumulative rotor angle and z, showing processive supercoiling during a single gyrase binding event (1 mM ATP, 0.8 pN tension). **d**–**f**, State transitions between Ω, α and ν are detected on the basis of fits to the angle trace (black line) and application of a threshold to the z trace (dashed horizontal line). **d**, 75 μM ATP, 0.8 pN tension; **e**, no nucleotide, 0.8 pN tension; **f**, 2 mM ATP, 1.4 pN tension. Dwells in the ν state were scored when z was contracted by less than 15 nm. A total of 1,415 gyrase encounters such as those shown in **c**–**f** were analyzed for this study; see Supplementary Table 4 for detailed statistics.

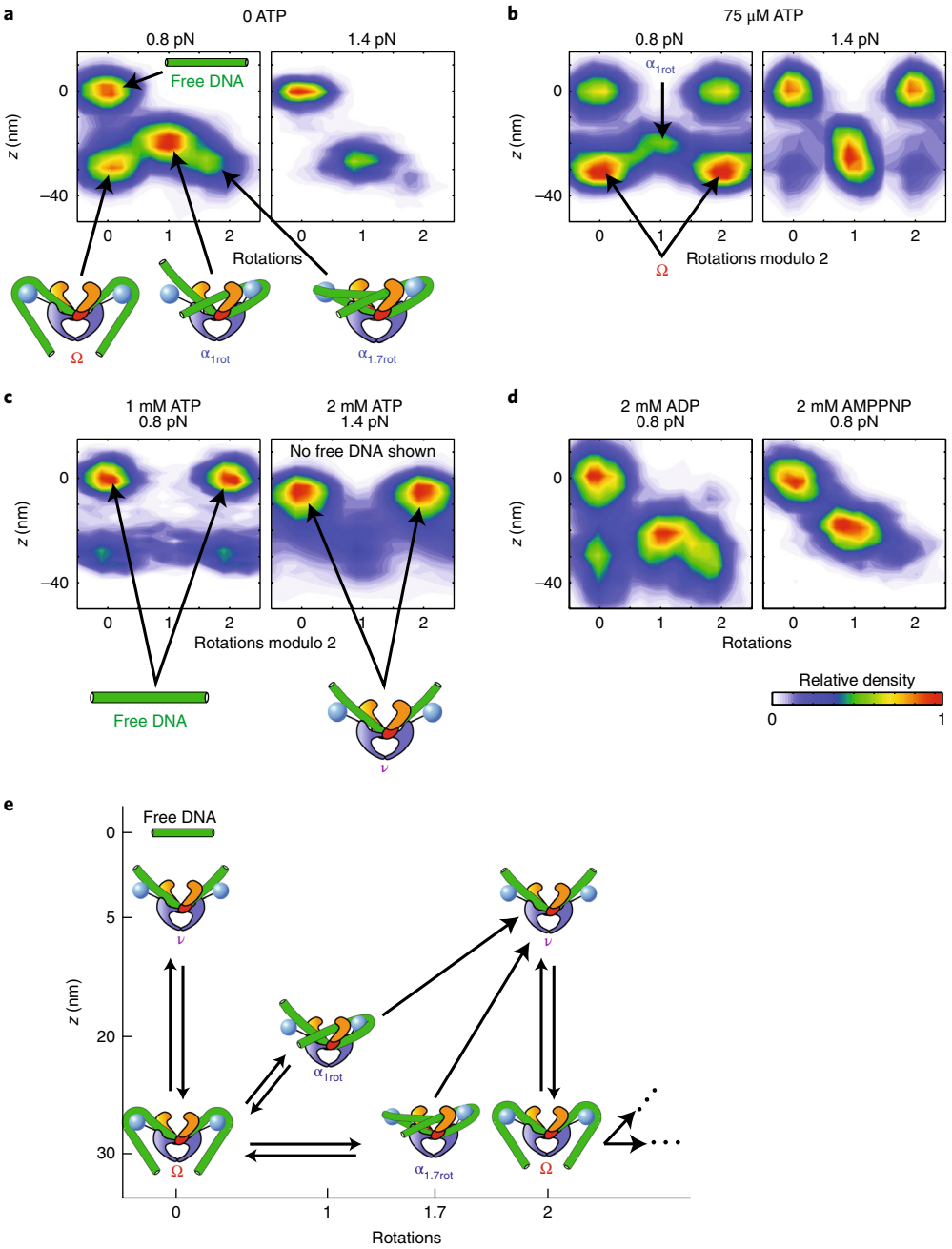

Fig. 2 | Conformations of the DNA:gyrase complex probed using RBT. a–d, Distributions of DNA:gyrase conformations under varying nucleotide and tension conditions. Gyrase binding events, together with flanking data reflecting free DNA (unless otherwise indicated), were excised from angle and *z* traces and pooled to construct histograms of paired (angle, *z*) values. See also Supplementary Table 1. The number of gyrase encounters included in each histogram is as follows: **a**, *N* = 38 (0 ATP, 0.8 pN), *N* = 19 (0 ATP, 1.4 pN); **b**, *N* = 20 (75 μM ATP, 0.8 pN), *N* = 48 (75 μM ATP, 1.4 pN); **c**, *N* = 9 (1 mM ATP, 0.8 pN), *N* = 74 (2 mM ATP, 1.4 pN); **d**, *N* = 26 (2 mM ADP), *N* = 16 (2 mM AMPPNP). **e**, Diagram showing conformations of the nucleoprotein complex in the angle–*z* plane, together with state transitions (arrows) characterized in this study.

conformational states (Fig. 2a–d and Supplementary Table 1). With improved *z* measurements, we now find that the two distinct chirally wrapped configurations, α_{1rot} and $\alpha_{1.7rot}$, differ not only in the number of supercoils trapped but also in the extent of *z* contraction (Fig. 2a). We propose that the differences in both angle and *z* between α_{1rot} and $\alpha_{1.7rot}$ are explained by chiral wrapping around one or both CTDs, either of which is sufficient to present a T-segment (Fig. 2a, bottom).

Our RBT measurements also provide sufficient sampling to localize the *ν* state on the angle–*z* plane. With DNA under 1.4 pN tension and in the presence of 2 mM ATP, there is a population at ~0 rotations and contracted in *z* by ~7 nm (Fig. 2c and Supplementary Table 1). These values of angle and *z* are consistent with a simple planar bend in the path of DNA (Supplementary Fig. 1). We propose that these conditions have stabilized the previously observed *ν* state[17] and that this state contains a G-segment bend similar to that seen in crystal structures of the gyrase cleavage core or other type II topoisomerases in complex with DNA[21,22], without wrapping of flanking DNA around the CTDs, as depicted in the *ν* state cartoons in Figs. 1 and 2. Based on the measured change in extension, we used

approximate theoretical results[23] and comparisons to simulations[24] to estimate the bend angle in the ν state (Supplementary Fig. 1), yielding estimates in the range 111°–126°. These angles are slightly smaller than the 150° bend observed in crystal structures[21,22], larger than the 70° G-segment bend modeled in a cryoelectron microscopy study of the complete gyrase:DNA complex[13], and similar to bend angles measured for several type II topoisomerases using atomic force microscopy and fluorescence resonance energy transfer (FRET) approaches[25].

Tension or nucleotides can redistribute conformations. Tension may be expected to redistribute the relative populations of states that differ in the extent of DNA contraction, with high tension favoring less contracted states. We found that the ν state, which is substantially less contracted than α or Ω, was undetectable within our spatiotemporal resolution at 0.8 pN, but observed at 1.4 pN (Fig. 2c and Supplementary Table 1). In addition, having discovered that the α_{1rot} state was less contracted than $\alpha_{1.7rot}$ or Ω, we examined the relative populations of these three states under differing tensions (Fig. 2a,b). The relative population of α_{1rot} was indeed increased at elevated tension, as expected (Supplementary Table 1); the repartitioning is in approximate quantitative agreement with thermodynamic expectations (Supplementary Table 2).

Nucleotide conditions also redistribute the populations of observed states, illuminating how structural transitions may be coordinated with the ATPase cycle. In the absence of nucleotide, as seen earlier, 2D histograms show three interconverting species: Ω, α_{1rot} and $\alpha_{1.7rot}$ (Fig. 2a). Increasing [ATP] favored Ω when DNA was under low tension (0.8 pN), as in previous work. However, under high (1.4 pN) tension, we found that high [ATP] favored ν (Fig. 2c), providing the first evidence that the dynamics of this state are directly coupled with the nucleotide cycle. The non-hydrolyzable ATP analog AMPPNP stabilized α (Fig. 2d), consistent with predominantly trapping a T-segment in a locked N-gate to stabilize the chiral wrap. Finally, we found that ADP, unlike ATP or AMPPNP, did not change the population distribution between Ω and α with respect to the apo condition (Fig. 2a,d and Supplementary Table 3).

Figure 2e places all of the observed conformations in the angle–z plane and indicates possible nucleotide- and tension-dependent transitions between them. With this framework in hand, we proceeded to perform kinetic analysis to develop an underlying mechanistic model in which the dynamics of conformational transitions are coordinated with substeps in the ATPase cycle.

The rate-limiting transition distinguishes ATP from ADP. Gyrase substep dynamics were previously investigated under varying [ATP] alone[16]. Here we have observed active supercoiling while varying both [ATP] and [ADP], to examine the fundamental role of ADP release in the mechanochemical cycle (Fig. 3). In the absence of ADP, we observed an ATP concentration-dependent dwell at the ~0 rotation mark, as in earlier work[16]. With DNA under moderate tension (0.8 pN), ν states were not detected and the dwell at ~0 rotations was dominated by the Ω state. The length of this dwell (τ_0) decreased with increasing [ATP] (Fig. 3a). When ADP was included in dynamic supercoiling measurements, we found that increasing [ADP] primarily lengthened the Ω dwell at ~0 rotations (Fig. 3b), showing that the kinetics of chiral wrapping is affected by ADP occupancy, and consistent with competition between ADP and ATP for binding to the Ω state.

The Ω-to-α transition is accelerated by binding of two ATP molecules, but can proceed at a slow rate in absence of nucleotide[16]. We have shown that ADP can bind to Ω and slow the Ω-to-α transition, explained by preventing the fast pathway by competition with ATP. We further asked whether the presence of bound ADP has any effect on the ATP-independent slow rate of transition from Ω to α observed in the absence of nucleotides. We measured Ω-to-α transition kinetics in the presence of 2 mM ADP and in the apo state and found them to be indistinguishable (Supplementary Table 3).

The ability to distinguish ATP from ADP is central to the mechanisms of ATPase motors. Bulk experiments showed that strand passage in gyrase requires ATP and is not supported by ADP[26], implying that a step before completion of strand passage distinguishes ATP from ADP. In the context of our model (Fig. 1), this could have been the Ω-to-α transition, exit from α via strand passage, or both. We now conclude that both steps discriminate between ADP and ATP: ADP must be exchanged for ATP to allow rapid formation of the chiral wrap via the Ω-to-α transition, and ATP is also required for subsequent strand passage. Mechanistically, our results may be explained by an inability of ADP binding to drive N-gate closure. This conclusion agrees with solution FRET studies of N-gate dimerization, which found that both the apo and the ADP-bound complex reside in an open N-gate configuration, distinct from the closed N-gate configuration of the ATP-bound complex[27].

Kinetics of chiral wrapping depend on [ADP]/[ATP]. The Ω-to-α chiral wrapping transition can distinguish between ATP and ADP: ATP accelerates this transition while ADP, or absence of any nucleotide, supports the transition at about one-tenth the rate. The [ADP]- and [ATP]-dependent kinetics (Fig. 3c) may be quantitatively fit using an extension of a previous [ATP]-dependent model (Supplementary Fig. 4), in which the Ω state exists in an equilibrium between its apo form and all possible combinations of ATP- and ADP-bound forms, with binding equilibria for ATP and ADP defined by K_{ATP} and K_{ADP}, respectively (Fig. 3d, Table 1 and Methods). Only the Ω_{2ATP} state, with two bound ATP molecules, can access the fast pathway for conversion to α (with rate constant k_2), whereas all other nucleotide states of Ω can convert to α via the same slow nucleotide-independent pathway (with rate constant k_1). Because the kinetics of state transitions in the ADP-saturated enzyme is indistinguishable from that of the apo enzyme (Supplementary Table 3) and ADP does not support strand passage[26], we make the simplifying assumption that ADP has no effect on enzyme dynamics apart from site occlusion; we cannot rule out more complex models in which asymmetrically occupied enzymes (for example, 1 ATP + 1 ADP) have distinct kinetic properties.

ADP thus functions as a competitive inhibitor, as also reported earlier for DNA gyrase on the basis of bulk measurements[26]. This type of model predicts that the rate-limiting exit from Ω, and consequently the overall supercoiling velocity, should depend only on the [ADP]/[ATP] ratio over a large range of nucleotide conditions. Our data agree with this prediction: the supercoiling velocity collapses onto the same curve as a function of [ADP]/[ATP] under independent titration of either species over this broad range of concentrations (Fig. 3e). Finally, we found that bulk measurements of ATPase rates showed the same dependence on [ADP]/[ATP] as single-molecule supercoiling rates (Fig. 3e and Supplementary Fig. 3), as expected for tight coupling between ATP consumption and supercoiling.

The α state is prolonged in the absence of hydrolysis. We used the non-hydrolyzable analog AMPPNP to investigate the specific role of hydrolysis. On the basis of pre-steady-state kinetic measurements on the related yeast topo II enzyme[19], hydrolysis might be expected to accelerate strand passage in DNA gyrase, although it is not strictly required for this step. In our mechanochemical model, strand passage is required for forward progress from the chirally wrapped α state. We therefore predicted that binding of AMPPNP might cause long dwells in α attributable to delayed strand passage.

In the presence of high [ATP] and 300 μM AMPPNP, we indeed saw long dwells at the ~1 or ~1.7 rotation mark (Fig. 4a) corresponding to the α state. Owing to limited spatiotemporal resolution, only α dwells that are long enough to be discerned from adjacent

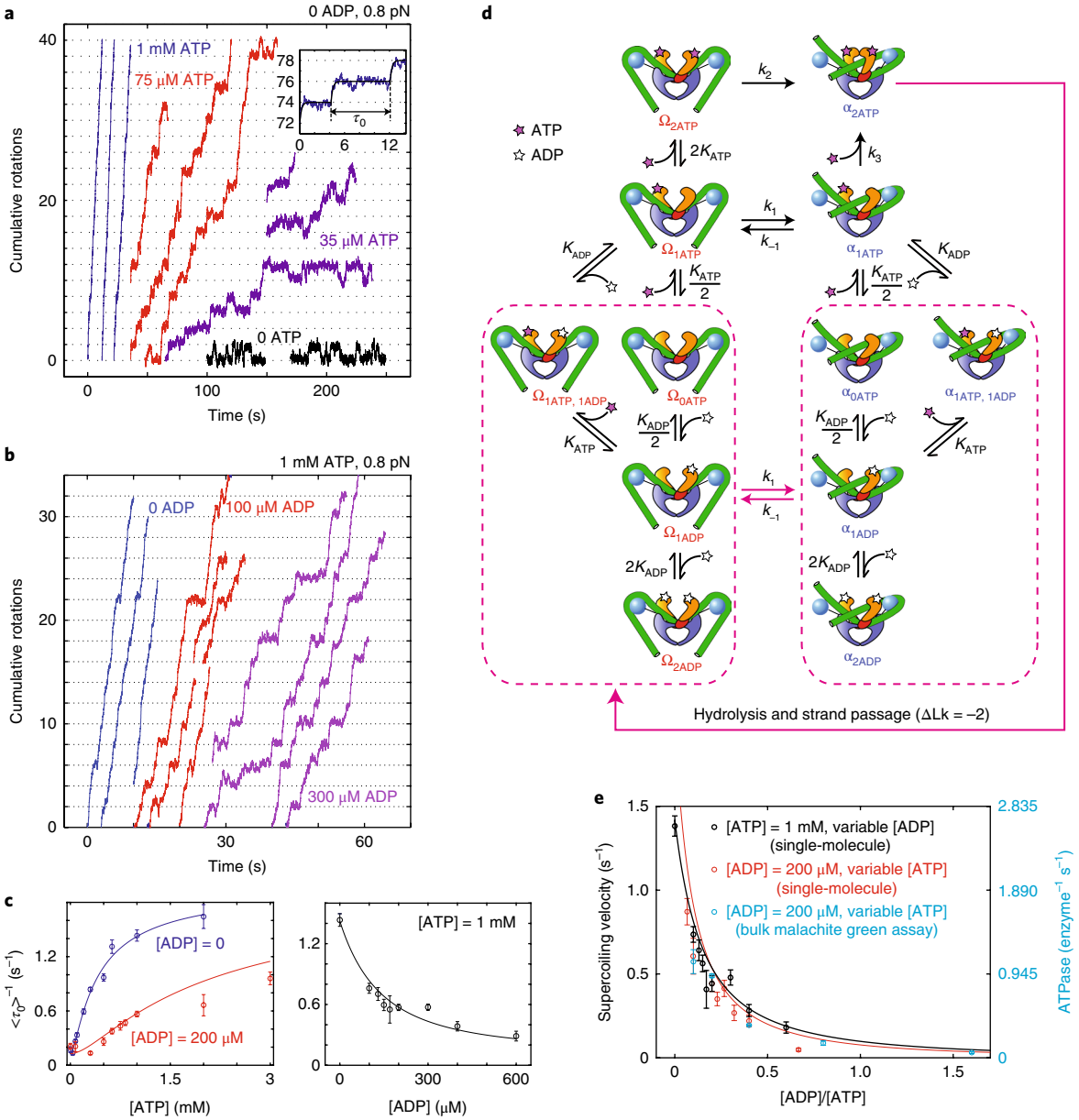

Fig. 3 | Structural dynamics of DNA gyrase associated with ADP/ATP exchange. All data were collected under 0.8 pN tension. **a**, Excised regions from traces of cumulative rotations as a function of time with varying [ATP]. Even rotations are indicated by dotted lines, in phase with the equilibrium value of angle before enzyme binding. Inset: after fitting angular traces to detect stepwise changes in equilibrium angle[16], τ_0 was defined as the duration of the major dwell at the ~0 rotation mark. **b**, Angular traces acquired in 1 mM ATP with varying [ADP]. See Supplementary Table 4 for the numbers of such angular traces N_{gyrase} analyzed for each condition in this study. **c**, [ATP] and [ADP] dependence of $<\tau_0>^{-1}$, where angle brackets denote the mean. Data are plotted as the inverse of the mean duration of the ~0 rotation dwell ± s.e.m. (see also Supplementary Fig. 2). See Supplementary Table 4 for the number of dwells N_0 averaged for each condition. Solid lines are fits to a mechanochemical model (**d**) in which the Ω state is modeled with all possible combinations of ATP and ADP binding in equilibrium to the two nucleotide binding pockets (see also Methods). The dissociation rate k_{off} from all Ω states is omitted from the diagram for simplicity. Reversible nucleotide binding transitions are modeled with single-site ATP and ADP affinities K_{ATP} and K_{ADP}, respectively; overall dissociation constants for binding transitions, incorporating site statistics due the presence of two independent binding sites, are indicated. Pink arrows connect sets of interconverting states grouped within pink dashed lines. Parameter values are quoted in Table 1. **e**, Dependence of supercoiling velocity on the [ADP]/[ATP] ratio. Data are coplotted for single-molecule RBT experiments in which either [ATP] (black) or [ADP] (red) was fixed, and bulk malachite green assays where [ADP] was fixed (cyan; see Supplementary Fig. 3). The solid lines are predictions of the model in **d**. Data are plotted as mean ± s.e.m. See Supplementary Table 4 for the number of cycle times N_{cycle} averaged for each single-molecule condition. For bulk experiments, three independent experiments were averaged for each data point.

angular dwells can be scored with confidence[16]. At moderate [ATP] in the absence of AMPPNP, observations of scored α states were rare and short-lived: at 1 mM ATP and 0 AMPPNP, the ratio of the number of scored dwells in α to the number of complete cycles was only 0.01 (3 of 220), with a mean dwell time in α of 0.5 ± 0.2 s. In contrast, after addition of 300 μM AMPPNP, the ratio of the number of scored dwells in α to the number of complete cycles was 0.22 (12 of 55), with a mean dwell time in α of 5 ± 2 s.

Under these conditions of added AMPPNP, the mean lifetime of scored dwells in α (Fig. 4a) averaged over all observed

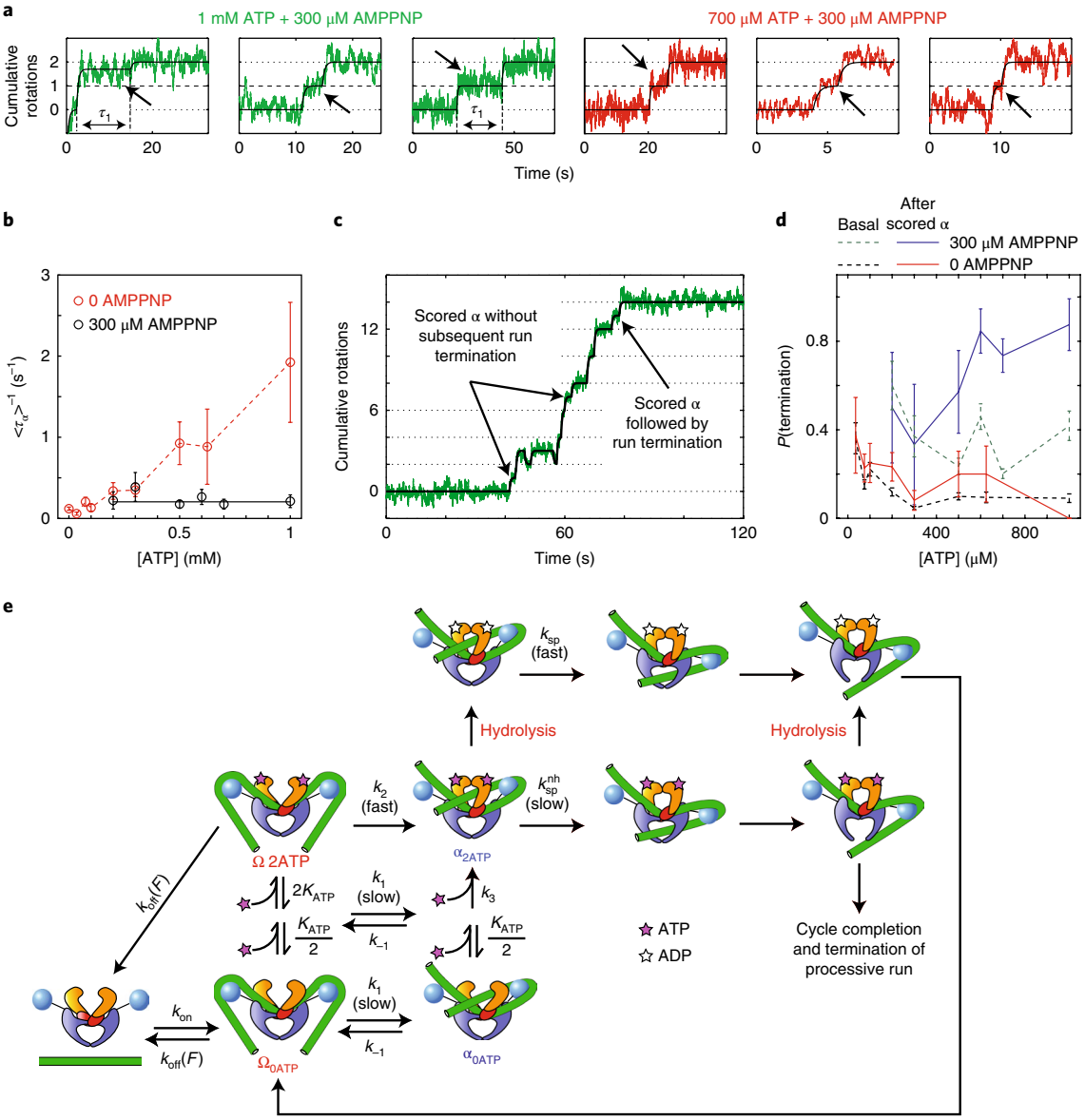

Fig. 4 | Structural dynamics of DNA gyrase associated with ATP hydrolysis. a, Excised regions from traces of cumulative rotations as a function of time in the presence of indicated [ATP] and 300 μM AMPPNP, illustrating long dwells in the chirally wrapped α state (arrows). **b**, [ATP] dependence of the rate of exit from α states ($<\tau_\alpha>^{-1}$) in absence of AMPPNP (red) and in presence of 300 μM AMPPNP (black). $<\tau_\alpha>$ is related to measurable quantities by $<\tau_\alpha> = <\tau_1 - \delta>$, where τ_1 is the duration of the ~1 or ~1.7 rotation dwell and δ is the detection threshold. Dwells at ~1 and ~1.7 rotations were scored by automated analysis only if they exceeded a detection threshold of 1 s or 4 s, respectively, allowing discrimination from adjacent major dwells. The abscissa of the horizontal black line is $<\tau_\alpha>^{-1}$ averaged over all [ATP] conditions. Data are plotted as inverse of the mean lifetime in the α state ± s.e.m. See also Supplementary Fig. 5. **c**, Two categories of on-pathway α states can be observed: those followed by completion of a single cycle and dissociation from the subsequent angular plateau and those followed by completion of the cycle and further Ω-to-α transitions. **d**, [ATP]-dependent probability that a scored on-pathway α state is followed by termination of the processive run (solid lines). Dashed lines represent the basal probability that any cycle is followed by dissociation, which is identical to $1 - P_T$, where P_T is the transition processivity (see Methods and Supplementary Fig. 4). Probabilities are plotted ± standard error $\sqrt{\frac{p(1-p)}{n}}$. **e**, Branched mechanochemical model. After formation of an α state with two ATPs bound, hydrolysis can accelerate strand passage, which occurs with rate k_{sp}. In the absence of ATP hydrolysis, the enzyme can still access a slower pathway for strand passage with rate k_{sp}^{nh}, after which it is incapable of processively beginning another cycle. *F* denotes the tension in the DNA tether. See Supplementary Table 4 for detailed statistics of the number of gyrase encounters N_{gyrase} analyzed for each condition in presence of 300 mM AMPPNP (**a**,**c**), the number of α dwells N_α averaged for each lifetime measurement (**b**) and the number of on-pathway α dwells $N_{\alpha,on}$ used for each probability measurement (**d**).

concentrations of ATP was 4.9 ± 0.9 s (N = 110), closely matching the slow rate of strand passage in the absence of hydrolysis measured for yeast topo II[19]. The duration of these dwells was independent of [ATP] (Fig. 4b), suggesting that ATP and AMPPNP do not rapidly exchange in α and that binding of AMPPNP specifically lengthens α by slowing the rate of exit from α via strand passage.

Inhibiting hydrolysis terminates processive supercoiling. We further investigated how hydrolysis affects enzyme dynamics subsequent to strand passage. If hydrolysis is necessary for enzyme reset, then AMPPNP should inhibit processivity. In the presence of a mixture of ATP and AMPPNP, long dwells in α are an indicator of AMPPNP binding and should thus be predictive of processive run

termination. Indeed, in the presence of AMPPNP, we observe that scored on-pathway α states had an enhanced probability of being followed by termination of the processive run (Fig. 4c,d). Run termination could correspond to either enzyme dissociation or the formation of an inactive N-gate-locked DNA-associated intermediate. In controls in the absence of AMPPNP, there was no substantial difference between the probability that supercoiling would halt after a scored α state and the basal probability that any completed cycle would be the last cycle of the processive run.

Overall, our observations suggest a model in which preventing the hydrolysis of one or more bound ATPs slows forward progress from α via strand passage; the enzyme may then complete the cycle, but is prevented from successfully resetting to begin another cycle. We incorporate the roles of both ATP binding and hydrolysis into a mechanochemical model that contains repeated branching (Fig. 4e). First, the Ω-to-α transition can happen quickly when ATP is bound at both ATPase sites (or happens slowly otherwise); next, strand passage can happen quickly when ATP is hydrolyzed (or happens slowly otherwise); finally, hydrolysis of both ATPs is required for enzyme reset.

High [ATP] prolongs transient releases of DNA. Single-molecule measurements of nucleotide-dependent substep kinetics to date have focused on the dynamics of the Ω and α states. The ν state has been identified as an additional conformation in which DNA contour is transiently released from the enzyme[17], and we have now determined that this conformation contains only a central G-segment bend (Fig. 2c). The ν-to-Ω transition thus represents a global rearrangement of the nucleoprotein complex that results in the sequestration of most of the DNA contour involved in the subsequent Ω-to-α chiral wrapping transition. While earlier work has established that the Ω-to-α transition is accelerated by ATP binding[16], inadequate resolution has made it difficult to determine whether the ν-to-Ω transition is also modulated by ATP. Here we have shown that increasing tension stabilizes the ν state (Fig. 2c and Supplementary Table 1), providing a method for slowing and studying the nucleotide dependence of the ν-to-Ω transition.

When DNA is under higher tension (1.4 pN), increasing [ATP] from 1 mM to 2 mM lengthens the dwell τ_0—a trend opposite to what is observed at low tension (0.8 pN) (Fig. 5). Since ν states are stabilized under high tension and lie at ~0 rotations (Fig. 2c), τ_0 includes contributions from dwells in both ν and Ω under high tension while only Ω dwells contributes significantly to τ_0 under low tension. Hence, the opposite trend of the dependence of τ_0 on [ATP] at high tension may result from ν dwells having a dependence on [ATP] that differs qualitatively from the [ATP]-dependent dynamics of Ω.

We directly probed ATP-modulated dynamics of the ν state by analyzing the [ATP] dependence of the ν state lifetime. In these experiments, DNA was held at the higher tension value of 1.4 pN. We can identify ν states by the characteristic low z contraction and angle ~0 rotations (Fig. 5b). Decreasing [ATP] reduced the contribution of ν and increased the contribution of Ω to τ_0 (Fig. 5b). At lower tension, ν states were not detected (Supplementary Fig. 6). Estimation of the dwell times in ν (Fig. 1f) shows a decreasing rate of exit from the ν state (τ_ν^{-1}) with increasing [ATP] (Fig. 5c). As an apparent consequence of the opposing trends of [ATP]-dependent ν and Ω lifetimes, the overall supercoiling rate under high tension showed a non-monotonic dependence on [ATP] (Fig. 5c): at low ATP concentrations, ν states are short lived and Ω dominates the τ_0 dwell and the supercoiling rate, while the situation is reversed at high [ATP].

A coordination mechanism is disrupted at high tension. To explain the [ATP]-dependent kinetics of the ν state, we propose a model in which ATP binding to the ν state drives dimerization of the N-gate in the absence of a trapped T-segment. The enzyme must then go through a round of futile hydrolysis to reopen the gate. These unproductive cycles are ordinarily avoided at low tension due to rapid exit from the ν state. By stabilizing the ν state under high tension, we may have thus disrupted and uncovered a natural mechanism for ensuring efficient coupling between nucleotide cycles and supercoiling. Previous bulk measurements suggested that gyrase has a high fuel efficiency on relaxed DNA even at saturating ATP, hydrolyzing only 1–2 ATPs per cycle[26], in contrast to the reported inefficiency of 7–8 ATPs per cycle for yeast topo II under a saturating [ATP][28]. We further investigated coupling between ATP consumption and supercoiling by measuring bulk ATPase rates under varying [ATP] and comparing the measurements to single-molecule supercoiling velocities (Supplementary Figs. 3 and 5c). Scaled ATPase rates showed remarkable agreement with the 0.8 pN supercoiling velocities over a wide range of [ATP] (Fig. 5c), implying a fixed coupling ratio that must arise from a coordinated mechanism. The best fit scaling factor (1.23 ATPs per cycle for the NADH-coupled assay shown in Fig. 5c) likely represents a lower limit on the coupling ratio, as a result of the presence of inactive enzymes in the bulk assay[29]; our results are thus consistent with consumption of two ATPs per cycle.

To explain the fuel efficiency of DNA gyrase, we have previously hypothesized that the properties of the Ω state prevent N-gate closure even when ATP is bound[16]. This coordination enforces a sequence in which N-gate closure occurs only during or after the Ω-to-α transition and hence follows T-segment capture. We now propose that futile N-gate closure in the absence of a trapped T-segment is permitted during dwells in ν. Futile hydrolysis is necessary for the gate to reopen and allow formation of the Ω state. This kinetic model can quantitatively explain the observed [ATP]-dependent kinetics of gyrase under high tension (Fig. 5c,d and Methods) and leads to both low fuel efficiency and low velocity (Fig. 5c) at 1.4 pN relative to 0.8 pN.

The kinetic model in Fig. 5d predicts that preventing ATP hydrolysis under high tension can lock the enzyme in the ν_{2ATP} state awaiting ATP hydrolysis to reopen the N-gate. We have tested this prediction of the model by recording angle and z as a function of time under 1.4 pN tension (favoring ν states) in the presence of 75 μM AMPPNP (Supplementary Fig. 7a). We observed very long dwells lasting as much as ~1,000 s in states that were weakly contracted in z and lay at the ~0 rotation mark. Consistent with the model, we identify these as long dwells in ν awaiting N-gate opening, which is inhibited in the absence of hydrolysis (Supplementary Fig. 7b).

Table 1 | Values of parameters appearing in the mechanochemical model for DNA gyrase under 0.8 pN and 1.4 pN tension

Parameter	0.8 pN	1.4 pN
K_{ATP}	196 μM	196 μM
K_{ADP}	46 μM	
k_1	0.065 s^{-1}	0.14 s^{-1}
k_{-1}	0.12 s^{-1}	0.091 s^{-1}
k_2	1.9 s^{-1}	2.1 s^{-1}
k_3	0.0072 μM^{-1} s^{-1}	0.0072 μM^{-1} s^{-1}
k_{off}	0.064 s^{-1}	0.35 s^{-1}
k_7		2.0 s^{-1}
k_{-7}		0.020 s^{-1}
k_r		8.6 s^{-1}
k_8		0.57 s^{-1}

Values of parameters appearing in the mechanochemical model for DNA gyrase under 0.8 pN (Fig. 3) and 1.4 pN (Fig. 5) tension. K_{ATP} and K_{ADP} are single-site affinities for nucleotide binding modeled as rapid equilibria; effective rate constants k_1 through k_8 correspond to labeled transitions in the model figures.

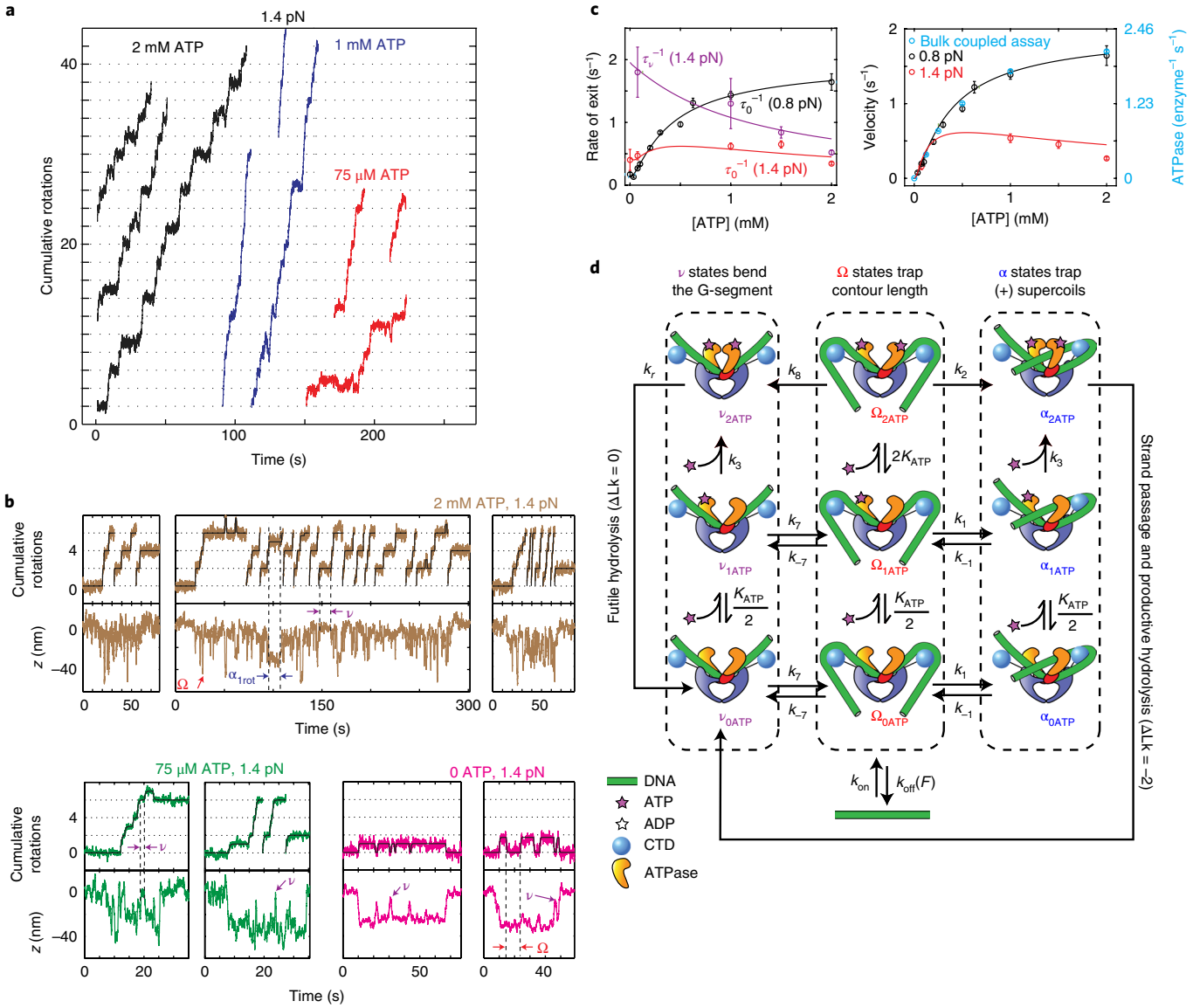

Fig. 5 | Structural dynamics of DNA gyrase affected by tension, and [ATP]-dependent analysis of the ν state. a, Excised angular traces under 1.4 pN tension. **b**, Angle and *z* measured under varying [ATP] and 1.4 pN tension. **c**, [ATP] dependence of τ_ν^{-1}, τ_0^{-1} and the overall supercoiling velocity, comparing 1.4 pN and 0.8 pN conditions (see also Supplementary Fig. 5). ATPase rates measured using a bulk NADH-coupled assay (Supplementary Fig. 3) are plotted with supercoiling velocity data. Data are plotted as inverse of the mean dwell time ± s.e.m. (left), mean velocity ± s.e.m. (right, bulk measurements) or inverse of the mean cycle time ± s.e.m. (right, single-molecule measurements). Solid lines are fits to a mechanochemical model (**d**) incorporating the ν state. Reversible ATP binding transitions are modeled with single-site affinity K_{ATP}. Some reverse transitions are ignored because of fast forward progress. All kinetic parameters other than K_{ATP} and k_3 have been allowed to vary from values determined at 0.8 pN and have been determined using measurements of processivities, state lifetimes and branching ratios (see Methods). Parameter values are quoted in Table 1. See Supplementary Table 4 for the number of gyrase encounters (**a**,**b**) analyzed for each condition and for the numbers of ν dwells, ~0 rotation dwells and cycle times averaged for each lifetime or supercoiling velocity measurement (**c**). For the bulk coupled assay, three independent measurements were made at each [ATP] (see Supplementary Fig. 3 for a plot of individual observations).

Discussion

Here we have measured structural dynamics and mechanochemical coupling in the gyrase:DNA complex, establishing both the geometries of conformational intermediates and the substeps in fuel consumption that drive transitions between them. We have mapped out a heavily branched kinetic pathway that underlies motor function. The proposed coupling mechanisms may be visualized in a landscape representation[30], wherein each nucleotide state gives rise to a distinct free energy surface as a function of mechanical coordinates (Supplementary Fig. 8).

Large-scale DNA:protein interactions are repeatedly formed, broken and rearranged during the gyrase cycle. Our measurements suggest that the DNA is bent around both CTDs in the Ω state, chirally wrapped around one CTD in α_{1rot} or both CTDs in $\alpha_{1.7rot}$, and released from both CTDs in the ν state (Fig. 2). High-resolution structures of intact gyrase bound to its complete DNA substrate in functional conformations are yet to be obtained. A model based on a low-resolution cryoelectron microscopy reconstruction[13] of a stabilized conformation resembles our depiction of $\alpha_{1.7rot}$, but the length of included DNA appears to be insufficient to present a

T-segment. The ν state, which we have here shown to be stabilized by ATP (Fig. 5) or AMPPNP (Supplementary Fig. 7) and to exhibit the extension signature expected for a simple planar bend (Fig. 2c and Supplementary Fig. 1), may most closely resemble a reported structure of *Saccharomyces cerevisiae* topo II in the presence of DNA and AMPPNP, showing a bent G-segment and closed N-gates in the absence of a T-segment[31].

While molecular motors are stochastic machines, they have evolved coordination mechanisms to favor ordered progression and efficient fuel consumption. Our measurements of ν state kinetics (Fig. 5) support a model[16] for coordination between N-gate closure and T-segment capture in the Ω state. Rapid ν-to-Ω transition protects the enzyme from premature closure of the N-gate. Without this coordination, hydrolysis is decoupled from strand passage, compromising both fuel efficiency and overall supercoiling velocity. Examples of coordination between the DNA conformation and the N-gate have also been seen in prior studies[31,32], including FRET studies revealing that chiral wrapping of DNA around the C-terminal domain induces narrowing of the N-gate[27].

The response of a molecular motor to mechanical and chemical perturbations not only reveals fundamental coupling mechanisms, but also provides insight into regulatory mechanisms available to the cell. Very modest changes in DNA tension are seen here (Fig. 5) and in previous work[33,34] to have dramatic effects on gyrase function and may be used to regulate gyrase in the chromosome. Moreover, the effect of the [ADP]/[ATP] ratio on gyrase substep dynamics (Fig. 3) suggests a mechanism underlying a long-appreciated link between cellular energy stores, genomic supercoiling and specific gene expression programs. Supercoiling has been proposed to act as a secondary messenger that transmits information about the environment to regulatory networks in the cell[6,34,35]. Changes in the intracellular [ADP]/[ATP] ratio—which reflect changes in cellular metabolism induced by environmental factors such as nutrient availability[36], oxygen[37] and osmotic shock—trigger changes in the superhelical density of the genome. This change in turn alters gene expression patterns[6,10] to help the cell adapt to the new environmental conditions. A possible role for gyrase in creating a dependence of the superhelical density on the [ADP]/[ATP] ratio, thus serving as a link between cellular metabolism and gene expression, has been recognized but not understood in mechanistic detail[38]. The physiological [ADP]/[ATP] ratio under various conditions in *E. coli* can lie between 0.06[39] and 0.5[40] or 1[37], coinciding with the sensitive region of the response curve we have experimentally explored (Fig. 3e). Gyrase thus is capable of sensing environmental conditions and adjusting the rate of a slow conformational step to throttle its supercoiling rate, which may consequently fine-tune the steady-state superhelicity that controls downstream transcriptional programs.

Single-molecule measurements of substep dynamics have previously revealed the detailed coupling mechanisms of only a handful of motors, including the P-loop motors F1 ATPase[41] and ϕ29 packaging motor[42]. Here we have observed substeps coupled to ATP binding, hydrolysis and product release in an archetypal member of the GHL ATPase family. To complete our understanding of gyrase mechanism, it will be important to determine the detailed three-dimensional architectures of the gyrase states described here, fully define the atomistic basis of allosteric transitions and investigate the possible role of alternative supercoiling mechanisms that require cleavage of only one DNA strand[43]. Future work will be needed to establish whether mechanisms of coupling and coordination are widely shared among the diverse family of GHL ATPases, which serve a wide range of functions from DNA repair to protein folding[44].

Methods

Methods, including statements of data availability and any associated accession codes and references, are available at https://doi.org/10.1038/s41589-018-0037-0.

Received: 14 January 2017; Accepted: 21 February 2018;
Published online: 16 April 2018

References

1. Dutta, R. & Inouye, M. GHKL, an emergent ATPase/kinase superfamily. *Trends Biochem. Sci.* **25**, 24–28 (2000).
2. Saraste, M., Sibbald, P. R. & Wittinghofer, A. The P-loop—a common motif in ATP- and GTP-binding proteins. *Trends Biochem. Sci.* **15**, 430–434 (1990).
3. Schoeffler, A. J. & Berger, J. M. DNA topoisomerases: harnessing and constraining energy to govern chromosome topology. *Q. Rev. Biophys.* **41**, 41–101 (2008).
4. Basu, A., Parente, A. C. & Bryant, Z. Structural dynamics and mechanochemical coupling in DNA gyrase. *J. Mol. Biol.* **428**, 1833–1845 (2016).
5. Wang, J. C. Cellular roles of DNA topoisomerases: a molecular perspective. *Nat. Rev. Mol. Cell Biol.* **3**, 430–440 (2002).
6. Peter, B. J. et al. Genomic transcriptional response to loss of chromosomal supercoiling in *Escherichia coli*. *Genome Biol.* **5**, R87 (2004).
7. Chong, S., Chen, C., Ge, H. & Xie, X. S. Mechanism of transcriptional bursting in bacteria. *Cell* **158**, 314–326 (2014).
8. Pommier, Y., Leo, E., Zhang, H. & Marchand, C. DNA topoisomerases and their poisoning by anticancer and antibacterial drugs. *Chem. Biol.* **17**, 421–433 (2010).
9. Bustamante, C., Chemla, Y. R., Forde, N. R. & Izhaky, D. Mechanical processes in biochemistry. *Annu. Rev. Biochem.* **73**, 705–748 (2004).
10. Cheung, K. J., Badarinarayana, V., Selinger, D. W., Janse, D. & Church, G. M. A microarray-based antibiotic screen identifies a regulatory role for supercoiling in the osmotic stress response of *Escherichia coli*. *Genome Res.* **13**, 206–215 (2003).
11. van Workum, M. et al. DNA supercoiling depends on the phosphorylation potential in *Escherichia coli*. *Mol. Microbiol.* **20**, 351–360 (1996).
12. Brown, P. O. & Cozzarelli, N. R. A sign inversion mechanism for enzymatic supercoiling of DNA. *Science* **206**, 1081–1083 (1979).
13. Papillon, J. et al. Structural insight into negative DNA supercoiling by DNA gyrase, a bacterial type 2A DNA topoisomerase. *Nucleic Acids Res.* **41**, 7815–7827 (2013).
14. Gubaev, A. & Klostermeier, D. The mechanism of negative DNA supercoiling: a cascade of DNA-induced conformational changes prepares gyrase for strand passage. *DNA Repair (Amst.* **16**, 23–34 (2014).
15. Bryant, Z., Oberstrass, F. C. & Basu, A. Recent developments in single-molecule DNA mechanics. *Curr. Opin. Struct. Biol.* **22**, 304–312 (2012).
16. Basu, A., Schoeffler, A. J., Berger, J. M. & Bryant, Z. ATP binding controls distinct structural transitions of *Escherichia coli* DNA gyrase in complex with DNA. *Nat. Struct. Mol. Biol.* **19**, 538–546 (2012).
17. Lebel, P., Basu, A., Oberstrass, F. C., Tretter, E. M. & Bryant, Z. Gold rotor bead tracking for high-speed measurements of DNA twist, torque and extension. *Nat. Methods* **11**, 456–462 (2014).
18. Gore, J. et al. Mechanochemical analysis of DNA gyrase using rotor bead tracking. *Nature* **439**, 100–104 (2006).
19. Baird, C. L., Harkins, T. T., Morris, S. K. & Lindsley, J. E. Topoisomerase II drives DNA transport by hydrolyzing one ATP. *Proc. Natl. Acad. Sci. USA* **96**, 13685–13690 (1999).
20. Schwenkert, S., Hugel, T. & Cox, M. B. The Hsp90 ensemble: coordinated Hsp90-cochaperone complexes regulate diverse cellular processes. *Nat. Struct. Mol. Biol.* **21**, 1017–1021 (2014).
21. Dong, K. C. & Berger, J. M. Structural basis for gate-DNA recognition and bending by type IIA topoisomerases. *Nature* **450**, 1201–1205 (2007).
22. Bax, B. D. et al. Type IIA topoisomerase inhibition by a new class of antibacterial agents. *Nature* **466**, 935–940 (2010).
23. Kulić, I. M., Mohrbach, H., Lobaskin, V., Thaokar, R. & Schiessel, H. Apparent persistence length renormalization of bent DNA. *Phys. Rev. E* **72**, 041905 (2005).
24. Vologodskii, A. Determining protein-induced DNA bending in force-extension experiments: theoretical analysis. *Biophys. J.* **96**, 3591–3599 (2009).
25. Hardin, A. H. et al. Direct measurement of DNA bending by type IIA topoisomerases: implications for non-equilibrium topology simplification. *Nucleic Acids Res.* **39**, 5729–5743 (2011).
26. Sugino, A. & Cozzarelli, N. R. The intrinsic ATPase of DNA gyrase. *J. Biol. Chem.* **255**, 6299–6306 (1980).
27. Gubaev, A. & Klostermeier, D. DNA-induced narrowing of the gyrase N-gate coordinates T-segment capture and strand passage. *Proc. Natl. Acad. Sci. USA* **108**, 14085–14090 (2011).
28. Lindsley, J. E. & Wang, J. C. On the coupling between ATP usage and DNA transport by yeast DNA topoisomerase II. *J. Biol. Chem.* **268**, 8096–8104 (1993).
29. Yasuda, R., Noji, H., Kinosita, K. Jr. & Yoshida, M. F1-ATPase is a highly efficient molecular motor that rotates with discrete 120 degree steps. *Cell* **93**, 1117–1124 (1998).

30. Wang, H. & Oster, G. Energy transduction in the F1 motor of ATP synthase. *Nature* **396**, 279–282 (1998).
31. Schmidt, B. H., Osheroff, N. & Berger, J. M. Structure of a topoisomerase II-DNA-nucleotide complex reveals a new control mechanism for ATPase activity. *Nat. Struct. Mol. Biol.* **19**, 1147–1154 (2012).
32. Tretter, E. M. & Berger, J. M. Mechanisms for defining supercoiling set point of DNA gyrase orthologs: I. A nonconserved acidic C-terminal tail modulates *Escherichia coli* gyrase activity. *J. Biol. Chem.* **287**, 18636–18644 (2012).
33. Fernández-Sierra, M., Shao, Q., Fountain, C., Finzi, L. & Dunlap, D. *E. coli* gyrase fails to negatively supercoil diaminopurine-substituted DNA. *J. Mol. Biol.* **427**, 2305–2318 (2015).
34. Nöllmann, M. et al. Multiple modes of *Escherichia coli* DNA gyrase activity revealed by force and torque. *Nat. Struct. Mol. Biol.* **14**, 264–271 (2007).
35. Dorman, C. J. Regulation of transcription by DNA supercoiling in *Mycoplasma genitalium*: global control in the smallest known self-replicating genome. *Mol. Microbiol.* **81**, 302–304 (2011).
36. Dorman, C. J. Genome architecture and global gene regulation in bacteria: making progress towards a unified model? *Nat. Rev. Microbiol.* **11**, 349–355 (2013).
37. Hsieh, L. S., Burger, R. M. & Drlica, K. Bacterial DNA supercoiling and [ATP]/[ADP]. Changes associated with a transition to anaerobic growth. *J. Mol. Biol.* **219**, 443–450 (1991).
38. Westerhoff, H. V., O'Dea, M. H., Maxwell, A. & Gellert, M. DNA supercoiling by DNA gyrase. A static head analysis. *Cell Biophys.* **12**, 157–181 (1988).
39. Bennett, B. D. et al. Absolute metabolite concentrations and implied enzyme active site occupancy in *Escherichia coli*. *Nat. Chem. Biol.* **5**, 593–599 (2009).
40. Hsieh, L. S., Rouviere-Yaniv, J. & Drlica, K. Bacterial DNA supercoiling and [ATP]/[ADP] ratio: changes associated with salt shock. *J. Bacteriol.* **173**, 3914–3917 (1991).
41. Adachi, K. et al. Coupling of rotation and catalysis in F_1-ATPase revealed by single-molecule imaging and manipulation. *Cell* **130**, 309–321 (2007).
42. Chistol, G. et al. High degree of coordination and division of labor among subunits in a homomeric ring ATPase. *Cell* **151**, 1017–1028 (2012).
43. Gubaev, A., Weidlich, D. & Klostermeier, D. DNA gyrase with a single catalytic tyrosine can catalyze DNA supercoiling by a nicking-closing mechanism. *Nucleic Acids Res.* **44**, 10354–10366 (2016).
44. Thomsen, N. D. & Berger, J. M. Structural frameworks for considering microbial protein- and nucleic acid-dependent motor ATPases. *Mol. Microbiol.* **69**, 1071–1090 (2008).

Acknowledgements

This work was supported by National Institutes of Health R01 grants GM106159 to Z.B. and CA077373 to J.M.B., a Stanford Bio-X Graduate Fellowship to A.B. and a Stanford Interdisciplinary Graduate Fellowship to P.M.L. NIH training grant 5T32GM008403-24 supported M.H.

Author contributions

A.B. designed and performed single-molecule experiments, analyzed single-molecule data and carried out theoretical modeling. M.H. designed and performed bulk biochemical experiments. A.B., P.L. and L.E.F. developed and characterized single-molecule tools and methods. M.H. and E.M.T. provided purified proteins. A.B., Z.B. and M.H. wrote the paper. All authors commented on the paper and discussed the results. Z.B. and J.M.B. supervised research.

Competing interests

The authors declare no competing financial interests.

Additional information

Supplementary information is available for this paper at https://doi.org/10.1038/s41589-018-0037-0.

Reprints and permissions information is available at www.nature.com/reprints.

Correspondence and requests for materials should be addressed to Z.B.

Publisher's note: Springer Nature remains neutral with regard to jurisdictional claims in published maps and institutional affiliations.

Methods

Preparation of DNA, proteins and beads. DNA constructs for RBT containing a variant of the μ phage strong gyrase site[45] were prepared as described previously[16]. Magnetic beads were prepared by crosslinking 1-μm carboxy-modified superparamagnetic beads (MyOne, Invitrogen) with rabbit anti-fluorescein (Invitrogen A889)[16,18]. Rotor beads were Power-Bind* streptavidin-coated polystyrene spheres (Thermo Scientific; 300-nm beads). *E. coli* GyrA and GyrB subunits were individually expressed and purified as described[32] (Supplementary Fig. 9), mixed to reconstitute tetramers and stored at −−80 °C in 50 mM Tris-HCl, pH 7.5, 100 mM potassium glutamate, 2 mM DTT, 1 mM EDTA and 10% (v/v) glycerol.

Bulk ATPase assays. DNA-stimulated ATPase activity was measured with 200 nM gyrase tetramer in the presence of saturating sheared salmon sperm DNA (100 ng/μl) in GB (35 mM Tris-HCl pH 7.8, 24 mM potassium glutamate, 2 mM DTT, 0.25 mg/ml BSA, 0.2 mM spermidine, 0.1% Tween-20 and 8 mM $MgCl_2$ with additional equimolar $MgCl_2$ included for concentrations of ATP above 1 mM). Two different assay methods were used: (i) an established enzyme-coupled assay[46] was used to characterize ATPase as a function of [ATP] with high signal-to-noise ratio, and (ii) since the enzyme-coupled assay regenerates ATP from ADP, a malachite green assay[47] was used to compare ATPase kinetics in the presence and absence of ADP. For both assays, measurements were performed in 75-μL reactions conducted in triplicate at 25 °C.

In the enzyme-coupled assay, ATP regeneration is coupled to the oxidation of NADH. The ATP-regeneration/NADH-oxidation system consisted of 2 mM phosphoenol pyruvate (PEP), 0.2 mM NADH and excess pyruvate kinase and lactate dehydrogenase enzyme mix (Sigma). The rate of ATP hydrolysis was measured as the decrease in the absorption at 340 nm using a CLARIOStar plate reader and fit to a linear model assuming one NADH is consumed for each ATP hydrolyzed.

In the malachite green assay, ATPase activity is measured by detecting free phosphate. After a 10-min incubation, 175 μL of malachite green reagent (0.034% malachite green, 10 mm ammonium molybdate, 1 N hydrochloric acid, 3.4% ethanol and 0.01% Tween-20) was added to each reaction and incubated at room temperature in the dark for 5 min. Malachite green molybdate complexes with free phosphate, creating a product that absorbs strongly at 620 nm. To relate 620-nm absorption to phosphate concentration, we generated a standard curve using a CLARIOStar plate reader by measuring the absorbance at 620 nm while varying sodium phosphate concentration from 0 to 50 μM in assay buffer. To correct for free phosphate contained in our commercially bought ATP and ADP stocks, we also conducted set of measurements that were identical to our ATPase assay conditions but in the absence of gyrase. ATPase rates in units of μM s^{-1} were calculated by measuring the phosphate concentration at the end of the incubation time, accounting for the presence of free phosphate contributed by nucleotide stocks, and dividing by the incubation time.

Single-molecule assays. Flow chambers were assembled using Nescofilm gaskets and hole-punched coverslips, with the objective side of the coverslip spin-coated with 0.1% (w/v) nitrocellulose in amyl acetate. To prepare rotor–DNA complexes, polystyrene spheres were centrifuged, washed in 400 μL PB1 (5 mg ml^{-1} acetylated BSA (Invitrogen) in PBS (137 mM NaCl, 2.7 mM KCl, 10 mM Na_2HPO_4 and 2 mM KH_2PO_4, pH 7.5)), centrifuged, resuspended in PB1 to match their original suspended volume, sonicated (20 min), and incubated (1 h) with DNA (~5 pM). Chambers were incubated with 0.79 μg ml^{-1} anti-digoxigenin (Roche 11333089001) in PBS (30 min), washed with 400 μL PB1 and incubated in PB1 (1 h) followed by rotor–DNA complexes (1 h). Chambers were then washed with 400 μL PB1, incubated with magnetic beads in PB1 (30 min) and finally washed with 400 μL of 0.5 mg ml^{-1} BSA (NEB) in PBS. Gyrase tetramer (0.6–6 nM) was added in GB containing the indicated ATP, ADP and AMPPNP concentrations. Phosphocreatine and creatine phosphokinase (Calbiochem) were added to final concentrations of 10 mM and 1.23 μM, respectively, for the purpose of ATP regeneration, except in cases where external ADP was added. When ADP was added, all data were collected in the first ~20 min after mixing gyrase with ATP.

Instrumentation. The instrumentation and methods for data collection and drift stabilization were adapted from those reported earlier[17]. Magnetic tweezers were implemented on a modified Nikon TE2000 inverted microscope. The polystyrene bead was imaged via evanescent scattering using an intensity-stabilized, 845-nm fiber-coupled single-mode diode laser (Lumics) as a source. A custom mount was used to support small, diametrically opposed mirrors below the back pupil of the microscope objective (Nikon 60×/1.49 TIRF) to introduce the laser excitation and subsequently remove the totally internally reflected return beam. The return beam was directed onto a position-sensitive detector (PSD) (Pacific Silicon) to provide a signal for focus stabilization using an *xyz* piezo stage (Mad City Labs). The scattered light from the rotor was imaged through an optical path splitter (Cairn, Optosplit II) onto an EMCCD camera (Andor iXon DV860).

Data acquisition and PSF fitting. Rotor bead images were recorded at 250 Hz. A quasi-real-time acquisition and analysis loop was run in Matlab at a loop rate of 1 Hz. During each loop, all available images were downloaded from the camera and fit using a 2D Gaussian fitting function, which was written in C and compiled as a Matlab executable. Fit parameters included an additive offset c, peak height A, x position x_0, y position y_0, x s.d. σ_x and y s.d. σ_y.

$$f = c + Ae^{\left(-\frac{(x-x_0)^2}{2\sigma_x^2}-\frac{(y-y_0)^2}{2\sigma_y^2}\right)}$$

Angle and *z* measurement. The rotor bead angle was determined by computing the four-quadrant inverse tangent of each corrected pair of (x,y) coordinates and then unwrapping the result to determine the cumulative angle. DNA tethers showing unconstrained rotor bead angles or sticking of the rotor bead were rejected from further analysis. The rotor bead height (z) was determined using evanescent nanometry as described previously[17], using $\Delta z = -\Lambda \log(I/I_0)$ where I is the instantaneous scattering intensity as determined by the 2D Gaussian fit ($I \equiv A\sigma_x\sigma_y$) and I_0 is the intensity at an arbitrary reference z height. The decay length Λ was calibrated using dual focus imaging as described previously[17].

Spatiotemporal resolution. Thermal fluctuations of harmonically constrained rotors are described by an angular variance $<\Delta\theta^2> = kT/\kappa$ and a relaxation time $\tau = \gamma/\kappa$, where κ is the torsional stiffness of the tether and γ is the rotational drag of the rotor. The value of τ was obtained by fitting the mean square deviation of the rotor angle as described[16]. At 0.8 pN, we measured $<\Delta\theta^2> = 3.8 \pm 0.6$ rad^2 and $\tau = 0.23 \pm 0.06$ s (mean ± s.d., $N = 10$). At 1.4 pN, we measured $<\Delta\theta^2> = 3.7 \pm 0.5$ rad^2 and $\tau = 0.24 \pm 0.06$ s (mean ± s.d., $N = 10$). These values are similar to the values obtained earlier using fluorescent rotors[16].

Substep analysis. The angular trace was modeled as a series of stepwise changes in the equilibrium rotor angle as described previously[16]. The instantaneous rotor angle follows the equilibrium angle with a lag, modeled as an exponential relaxation with the characteristic decay time τ determined independently for each rotor as described above. Step locations were obtained by least-squares fitting, assuming that each forward cycle contains a dwell at 0 rotations and may contain either a detectable (>1 s) dwell at 1 rotation, a detectable (>4 s) dwell at 1.7 rotations, or no detectable midcycle pause. The measured value of τ_1 was shifted by the detection limit cutoff to correct for undetected short pauses. To score ν states at 1.4 pN, first the dwells τ_0 were identified by fitting the angle trace. Subintervals within the dwell τ_0 where the amount of z contraction was less than 15 nm were identified as dwells in ν and other subintervals were identified as Ω. If two adjacent ν dwells within the same angular dwell τ_0 were separated by an Ω dwell where the amount of z contraction was less than 20 nm, then all three states were merged into a single ν dwell. Data for z shown in Fig. 5 and used for ν dwell analysis were downsampled using a moving average of 100 or 300 frames. Both of the extreme conditions used in ν lifetime estimation (at 75 μM and 2 mM ATP) were processed using 100 frame averaging, and model fit parameters were not substantially altered when only these lifetimes were included.

Occasionally, very long dwells were observed that may reflect paused states. To avoid substantial shifts in reported mean dwell times, we excluded these dwells from analysis for cases in which a single dwell time represented >30% of the total summed dwell times for a given condition containing $N > 15$ measurements. These criteria were satisfied only 3 times in the full dataset; in these cases, the corresponding trace was also removed from the associated angle-z 2D histogram.

Kinetic modeling of DNA gyrase at 0.8 pN tension. The kinetics of gyrase at 0.8 pN tension were calculated using the model depicted in Fig. 3d, which simplifies to the model depicted in Supplementary Fig. 4 in the absence of ADP and is closely adapted from previous work[16]. In these calculations, nucleotide binding transitions depicted with double arrows were approximated as rapid equilibria, modeled using dissociation constants only. Other transitions were modeled as rate processes using the labeled kinetic constants. The central feature of the model, retained from previous work, is a branched mechanism in which the Ω-to-α transition can occur via a fast pathway if and only if two ATP molecules are bound. The probability of having two bound ATP molecules depends on [ATP] and [ADP], calculated according to binding equilibria. In the current work, we model nucleotide binding assuming independent binding sites, relying only on the single-site dissociation constants K_{ATP} and K_{ADP}. Effective binding constants for transitions between nucleotide occupancies for the GyrB dimer may then be calculated on the basis of site statistics. For example, the transition between Ω_{0ATP} and Ω_{1ATP} is governed by an effective ATP dissociation constant of $K_{ATP}/2$. This may be understood by noting that Ω_{0ATP} has two available empty sites and thus an effective ATP binding rate of $2k_{on}$, while Ω_{1ATP} has only one bound ATP and thus an effective ATP dissociation rate of k_{off}, together giving an effective dissociation constant $K = k_{off}/2k_{on} = K_{ATP}/2$.

When ADP is omitted (Supplementary Fig. 4a), the rate of exit from Ω is given by

$$k_\Omega = \frac{k_2[ATP]^2}{[ATP]^2 + 2K_{ATP}[ATP] + K_{ATP}^2} + \frac{k_1(2K_{ATP}[ATP] + K_{ATP}^2)}{[ATP]^2 + 2K_{ATP}[ATP] + K_{ATP}^2} + k_{off}$$

and can be related to measurable quantities by $k_\Omega = <\tau_0>^{-1}$. Fitting the measured dependence of k_Ω on [ATP] to this expression (Supplementary Fig. 4b) yields values for the fitting parameters $k_2 + k_{off}$, $k_1 + k_{off}$ and K_{ATP}. The transition processivity, defined as the probability that an enzyme in Ω will transition to α before dissociation, is given by

$$P_T = 1 - \frac{k_{off}}{k_\Omega}$$

and can be related to measurable quantities by $P_T = 1 - <n_{fut} + n_{for}>^{-1}$, where n_{fut} and n_{for} are the number of futile excursions and forward steps, respectively, per processive burst, ignoring binding events for which $n_{fut} + n_{for} = 0$. Fitting the dependence of P_T on [ATP] to this expression (Supplementary Fig. 4c) yields a value for the parameter k_{off}. Taken together, the two fits in Supplementary Fig. 4 provided values for the parameters k_1, k_2, K_{ATP} and k_{off}. To obtain the remaining parameters of the model, we obtained k_{-1} as given by the measured value of k_α under apo conditions (Supplementary Table 3), set $2k_3/K_{ATP}$ to the value obtained earlier (previously[16] denoted k_3/K_3), and used this quantity together with the fit value K_{ATP} to calculate k_3.

Similar expressions can be written for the mechanochemical model in presence of ADP (Fig. 3d), with one additional parameter K_{ADP}, defined as the single-site dissociation constant for ADP. Equilibrium constants for transitions between nucleotide occupancies are again calculated using site statistics, assuming independent binding sites (Fig. 3d).

The [ATP] and [ADP] dependence of the rate of exit from Ω is given by

$$k_\Omega = k_{off} + k_2 P_{\Omega_{2ATP}} + k_1 (1 - P_{\Omega_{2ATP}})$$

where

$$P_{\Omega_{2ATP}} = K_{ADP}^2 [ATP]^2 \times \left(\begin{array}{l} K_{ATP}^2 K_{ADP}^2 + 2K_{ATP} K_{ADP}^2 [ATP] + K_{ADP}^2 [ATP]^2 + \\ 2K_{ATP}^2 K_{ADP} [ADP] + K_{ATP}^2 [ADP]^2 + 2K_{ATP} K_{ADP} [ADP][ATP] \end{array} \right)^{-1}$$

The value of K_{ADP} was obtained by fitting the data in Fig. 3c to this expression while keeping all other parameters fixed. All parameter values are quoted in Table 1.

The [ATP] and [ADP] dependence of the rate of exit from the α state is given by

$$k_\alpha = k_{-1} + k_3 [ATP] P_{\alpha_{1ATP}}$$

where

$$P_{\alpha_{1ATP}} = \frac{1}{1 + \frac{K_{ATP}}{2[ATP]} + \frac{[ADP]K_{ATP}}{[ATP]K_{ADP}} + \frac{[ADP]^2 K_{ATP}}{2[ATP]K_{ADP}^2} + \frac{[ADP]}{K_{ADP}}}$$

The [ATP] and [ADP] dependence of the overall supercoiling velocity V (equal to the inverse of the mean cycle time) may also be calculated from this model, yielding

$$V = \frac{1 - f_1 f_2}{\frac{1}{k_\Omega} + \frac{f_1}{k_\alpha}}$$

where

$$f_1 = \frac{k_1 (1 - P_{\Omega_{2ATP}})}{k_1 (1 - P_{\Omega_{2ATP}}) + k_2 P_{\Omega_{2ATP}}}$$

and

$$f_2 = \frac{k_{-1}}{k_{-1} + k_3 [ATP] P_{\alpha_{1ATP}}}$$

Supercoiling velocity was calculated from the parameters of the model without any further fitting, and is plotted in Figs. 3e and 5c.

Kinetic modeling of DNA gyrase at 1.4 pN tension. The parameters for the branched kinetic model for DNA gyrase with DNA under 1.4 pN tension (Fig. 5d) were determined by fitting model predictions to measurements of state lifetimes and statistics as a function of [ATP]. We first assumed that K_{ATP} and k_3 are independent of tension, and used parameters determined at 0.8 pN tension. k_{-1} was then set to the inverse of the mean lifetime of the α state at 0 ATP, $<\tau_1> = 11 \pm 3$ s ($N = 27$). To determine k_1, k_2, k_{-7}, k_8 and k_{off}, we then made use of the following expressions related to measurable quantities:

First, the transition processivity P_T can be expressed and related to measurements as above. At 2 mM ATP,

$$P_T = \frac{k_2 P_{\Omega_{2ATP}} + k_1 (1 - P_{\Omega_{2ATP}})}{k_2 P_{\Omega_{2ATP}} + k_1 (1 - P_{\Omega_{2ATP}}) + k_{off}} = 1 - <n_{fut} + n_{for}>^{-1}$$

where we measured $<n_{fut} + n_{for}> = 6.0 \pm 1.6$ ($N = 74$). At 0 ATP,

$$P_T = \frac{k_1}{k_1 + k_{off}} = 1 - <n_{fut}>^{-1}$$

where we measured $<n_{fut}> = 1.4 \pm 0.2 (N = 20)$

Second, an analogous ν branching ratio P_ν is defined as the probability that an enzyme in Ω will transition to ν rather than α. An expression for P_ν can be related to measurable quantities at 0 ATP:

$$P_\nu = \frac{k_{-7}}{k_1 + k_{-7}} = \frac{n_\nu}{n_\nu + n_\alpha}$$

where we measured $n_\nu = 4$ and $n_\alpha = 28$, the total number of ν and α states observed among all 20 traces at 0 ATP.

P_ν can be also be related to measurable quantities at 2 mM ATP:

$$P_\nu = \frac{k_8 P_{\Omega_{2ATP}} + k_{-7} (1 - P_{\Omega_{2ATP}})}{P_{\Omega_{2ATP}} (k_8 + k_2) + (1 - P_{\Omega_{2ATP}}) (k_1 + k_{-7})} = \frac{n_{\nu[rev]}}{n_{\nu[rev]} + n_{\tau_0}}$$

where $n_{\nu[rev]}$ counts only ν states that result from a reversion from Ω to ν rather than an on-pathway α-to-ν transition. We counted these states only approximately within the time resolution of our assay, by scoring ν states as reversion events if they occurred >2 s after the beginning of the cycle, yielding measured $n_{\nu[rev]} = 101$ and $n_{\tau_0} = 369$ dwells at the ~0 rotation mark among all 74 traces obtained at 2 mM ATP.

The rate of exit from Ω may be expressed as

$$k_\Omega = P_{\Omega_{2ATP}} (k_2 + k_8) + (1 - P_{\Omega_{2ATP}}) (k_1 + k_{-7}) + k_{off}$$

and was set equal to the inverse of the mean lifetime of ~0 rotation dwells that did not contain ν dwells. We measured $1/k_\Omega = 0.39 \pm 0.02$ s ($N = 112$) at 2 mM ATP.

After setting all other parameters by solving the equations above, we obtained k_r and k_7 by fitting τ_ν and τ_0 as a function of [ATP] to the corresponding mean first passage times calculated from the full kinetic model (Fig. 5c,d and Table 1). Supercoiling velocity was then calculated as the inverse of the mean cycle time from the full model without any further fitting.

Data collection statistics. For single-molecule measurements, a total of 1,415 gyrase encounters on 76 independent DNA tethers were analyzed for this study; a detailed breakdown of single-molecule statistics is provided in Supplementary Table 4. All bulk ATPase measurements were performed in triplicate (Supplementary Fig. 3).

Reporting Summary. Further information on experimental design is available in the Nature Research Reporting Summary linked to this article.

Data availability. Datasets generated for this study are available from the corresponding author upon reasonable request, including source data for the following panels: Figs. 1c–f, 2a–d, 3a–c,e, 4a–d and 5a–c and Supplementary Figs. 1, 2, 3, 4b,c, 5, 6 and 7.

Software and code availability. Data acquisition, analysis and real time feedback were carried out using custom scripts in Matlab (MathWorks) and C. Figures were prepared using Matlab and Adobe Illustrator. Scripts used for data acquisition and analysis are available from the corresponding author upon reasonable request. Code for a previous implementation of basic evanescent scattering rotor bead tracking data acquisition functions is available in the supplementary material for ref. [17].

References

45. Pato, M. L., Howe, M. M. & Higgins, N. P. A. DNA gyrase-binding site at the center of the bacteriophage Mu genome is required for efficient replicative transposition. *Proc. Natl. Acad. Sci. USA* **87**, 8716–8720 (1990).
46. Lindsley, J. E. Use of a real-time, coupled assay to measure the ATPase activity of DNA topoisomerase II. *Methods Mol. Biol.* **95**, 57–64 (2001).
47. Lanzetta, P. A., Alvarez, L. J., Reinach, P. S. & Candia, O. A. An improved assay for nanomole amounts of inorganic phosphate. *Anal. Biochem.* **100**, 95–97 (1979).

nature research

Corresponding author(s): Zev Bryant

☐ Initial submission ☐ Revised version ☒ Final submission

Life Sciences Reporting Summary

Nature Research wishes to improve the reproducibility of the work that we publish. This form is intended for publication with all accepted life science papers and provides structure for consistency and transparency in reporting. Every life science submission will use this form; some list items might not apply to an individual manuscript, but all fields must be completed for clarity.

For further information on the points included in this form, see Reporting Life Sciences Research. For further information on Nature Research policies, including our data availability policy, see Authors & Referees and the Editorial Policy Checklist.

Experimental design

1. Sample size

Describe how sample size was determined.	No predetermined sample size was used.

2. Data exclusions

Describe any data exclusions.	The Methods describe rejection of DNA tethers from analysis, rejection of short dwells with statistical correction, and exclusion of rare outlier dwells.

3. Replication

Describe whether the experimental findings were reliably reproduced.	Datasets acquired for repeated conditions were included in the analysis for this study, with statistics tabulated in the Supplementary Materials; none were considered failed attempts at replication.

4. Randomization

Describe how samples/organisms/participants were allocated into experimental groups.	N/A. This study does not involve animals or human subjects.

5. Blinding

Describe whether the investigators were blinded to group allocation during data collection and/or analysis.	N/A (no blinding). This study does not involve animals or human subjects.

Note: all studies involving animals and/or human research participants must disclose whether blinding and randomization were used.

6. Statistical parameters

For all figures and tables that use statistical methods, confirm that the following items are present in relevant figure legends (or in the Methods section if additional space is needed).

n/a	Confirmed	
☐	☒	The exact sample size (*n*) for each experimental group/condition, given as a discrete number and unit of measurement (animals, litters, cultures, etc.)
☐	☒	A description of how samples were collected, noting whether measurements were taken from distinct samples or whether the same sample was measured repeatedly
☐	☒	A statement indicating how many times each experiment was replicated
☒	☐	The statistical test(s) used and whether they are one- or two-sided (note: only common tests should be described solely by name; more complex techniques should be described in the Methods section)
☒	☐	A description of any assumptions or corrections, such as an adjustment for multiple comparisons
☒	☐	The test results (e.g. *P* values) given as exact values whenever possible and with confidence intervals noted
☐	☒	A clear description of statistics including central tendency (e.g. median, mean) and variation (e.g. standard deviation, interquartile range)
☐	☒	Clearly defined error bars

See the web collection on statistics for biologists for further resources and guidance.

Software

Policy information about availability of computer code

7. Software

Describe the software used to analyze the data in this study.	Data were analyzed using custom scripts in MATLAB (Mathworks).

For manuscripts utilizing custom algorithms or software that are central to the paper but not yet described in the published literature, software must be made available to editors and reviewers upon request. We strongly encourage code deposition in a community repository (e.g. GitHub). *Nature Methods* guidance for providing algorithms and software for publication provides further information on this topic.

Materials and reagents

Policy information about availability of materials

8. Materials availability

Indicate whether there are restrictions on availability of unique materials or if these materials are only available for distribution by a for-profit company.	All unique materials used are readily available from the authors.

9. Antibodies

Describe the antibodies used and how they were validated for use in the system under study (i.e. assay and species).	Antibodies were used only for attachment of DNA molecules to surfaces, following methods used previously in cited papers. Antibodies were obtained from commercial sources, and are identified by catalog number in the Methods.

10. Eukaryotic cell lines

a. State the source of each eukaryotic cell line used.	No eukaryotic cell lines were used.
b. Describe the method of cell line authentication used.	N/A
c. Report whether the cell lines were tested for mycoplasma contamination.	N/A
d. If any of the cell lines used are listed in the database of commonly misidentified cell lines maintained by ICLAC, provide a scientific rationale for their use.	N/A

Animals and human research participants

Policy information about studies involving animals; when reporting animal research, follow the ARRIVE guidelines

11. Description of research animals

Provide details on animals and/or animal-derived materials used in the study.	No animals were used.

Policy information about studies involving human research participants

12. Description of human research participants

Describe the covariate-relevant population characteristics of the human research participants.	The study did not involve human research participants.